



Full paper

K_{0.54}[Co_{0.5}Mn_{0.5}]O₂: New cathode with high power capability for potassium-ion batteries

Ji Ung Choi^{a,1}, Jongsoon Kim^{a,1}, Jang-Yeon Hwang^{b,1}, Jae Hyeon Jo^a, Yang-Kook Sun^{b,**},
Seung-Taek Myung^{a,*}

^a Department of Nanotechnology and Advanced Materials Engineering & Sejong Battery Institute, Sejong University, Seoul, 05006, South Korea

^b Department of Energy Engineering, Hanyang University, Seoul, 04763, South Korea



ARTICLE INFO

Keywords:

Layered
First-principles calculation
Cathode
Potassium
Battery

ABSTRACT

We propose P3-K_{0.54}[Co_{0.5}Mn_{0.5}]O₂, which is rationally designed as a promising cathode material for high-performance potassium-ion batteries (KIBs). Its composition adopts the use of the valence state of Mn above 3.5 + to minimize the disruptive effect of Jahn–Teller distortion in the MnO₆ octahedra during the electrochemical reaction. Unlike other types of layered materials that suffer from the sluggish diffusion of large potassium ions accompanying multi-step voltage profiles, P3-K_{0.54}[Co_{0.5}Mn_{0.5}]O₂ delivers a high specific discharge capacity of 120.4 mAh (g-oxide)⁻¹ with smooth charge and discharge curves. First-principles calculations predict an activation barrier energy of ~260 meV for a large K⁺ diffusion, which is comparable to those observed in conventional layered cathode materials for lithium-ion batteries. As a result, even at 500 mA g⁻¹, P3-K_{0.54}[Co_{0.5}Mn_{0.5}]O₂ is able to deliver a high discharge capacity of 78 mAh g⁻¹, which is a retention of 65% versus the capacity obtained at 20 mA g⁻¹. Combination studies using *operando* X-ray diffraction, the *ex-situ* X-ray absorption near-edge structure, and first-principles calculations elucidate the nature of the excellent potassium storage mechanism of K_{0.54}[Co_{0.5}Mn_{0.5}]O₂. This work provides a new insight for the development of efficient cathode materials for KIBs.

1. Introduction

To date, lithium-ion batteries (LIBs) have shown dominance in applications ranging from portable electronics to electric vehicles because of their high-energy density and satisfactory cycle life [1]. However, because of the abrupt increase in the demand for LIBs, the industry is facing a critical issue involving the potential shortage of lithium resources. This has shown the urgent need to develop new types of batteries to replace the present LIBs [2,3]. Recently, K-ion batteries (KIBs) have emerged as one of the possible alternatives to LIBs because of the abundance of potassium resources and similar standard electrode potential of potassium compared to those of lithium and sodium; namely, -3.04 V vs. a standard hydrogen electrode (SHE) for Li, -2.93 V vs. a SHE for K, and -2.71 V vs. a SHE for Na [4]. Moreover, it is known that potassium ions can be reversibly de/intercalated into the crystal structure of graphite-based materials [5], indicating the applicability of graphite-based carbonaceous materials as the anodes of KIBs. Thus, the established system for LIBs can be more smoothly transferred to KIBs.

Recently, many studies have been directed toward the development of novel cathode materials for KIBs [6–11]. In particular, layered Mn-based cathode materials, K_xMnO₂ (0 < x < 0.7), have been intensively investigated as promising cathodes because of their high theoretical capacities and low material cost [6,8–10]. Vaalma et al. [6] confirmed the feasibility of using orthorhombic P2 K_{0.3}MnO₂, which delivers a discharge capacity of 74 mAh g⁻¹ with stable cyclability in the range of 1.5–3.5 V. Later work by Kim et al. investigated K_{0.5}MnO₂ stabilized into a P3-type layered structure (R3m). The electrode performance had a discharge capacity of ~110 mAh g⁻¹ in the range of 1.5–3.9 V [8]. Mn was replaced by Fe, Ni, and Co elements. The co-substitution of Ni and Co in K_{0.67}[Ni_{0.17}Co_{0.17}Mn_{0.66}]O₂ seemed to make no difference in the capacity [9]. However, the resulting capacity retention was somehow improved over cycles. K_{0.7}[Fe_{0.5}Mn_{0.5}]O₂ utilized the redox pair of Fe^{4+/3+}. This gave the electrode a high discharge capacity of approximately 178 mAh g⁻¹, which was the highest value reported in KIBs [10]. In this case, the average oxidation state of Mn was 3.6+. However, the delivery of such a high charge capacity

* Corresponding author.

** Corresponding author.

E-mail addresses: yksun@hanyang.ac.kr (Y.-K. Sun), smyung@sejong.ac.kr (S.-T. Myung).

¹ These authors contributed equally to this paper.

($\sim 210 \text{ mAh g}^{-1}$) is still not fully understood because the combination of $\text{Fe}^{3+/4+}$ and $\text{Mn}^{3.6+/4+}$ redox pairs can theoretically contribute to the charge capacity of 182 mAh g^{-1} . It seems that unexpected oxidative decomposition of the electrolyte during charging may occur; otherwise, it is not possible to explain the reason based on the redox pairs of $\text{Fe}^{3+/4+}$ and $\text{Mn}^{3+/4+}$. With the exception of P'2 $\text{K}_{0.3}\text{MnO}_2$ [6], the P3 types of Mn-based cathode materials exhibit a phase transition toward the O3-type of layered structure at a highly depotassiated state as a result of multiphase transitions, which induce a large volume change. The diffusion of large potassium ions ($\sim 1.38 \text{ \AA}$) into/out of the K_xMnO_2 structure is likely to accompany the inevitable multiple phase transitions, which results in a non-smooth charge/discharge curve with such steps [6,8]. This may be the cause of the poor power capability of K_xMnO_2 . Moreover, the challenges faced in the application of Mn-based electrode materials should be resolved, including the presence of the Jahn–Teller (JT) distortion of Mn^{3+} that shows elongation of the Mn–O distance in one direction in the octahedral environment at a deeply potassiated (discharged) state.

These challenges must be overcome to mitigate the structural transition during de/potassiation and circumvent the structural disorder caused by the JT effect of Mn^{3+} in the crystal structure. In this work, the oxidation state of Mn is increased to 4+ by replacing half of the Mn with Co to obtain P3- $\text{K}_{0.54}[\text{Co}_{0.5}\text{Mn}_{0.5}]\text{O}_2$. As reported by Kim et al. [8], P3 type layered $\text{K}_{0.5}\text{MnO}_2$ delivers a discharge capacity $\sim 110 \text{ mAh g}^{-1}$ in the range of 1.5–3.9 V, accompanied by reversible multiphase transition of $\text{P3} \rightarrow \text{O3} \rightarrow \text{X}$ (O3-like phase). K^+ /vacancy ordering is the main factor to judge the voltage profile that shows multiple phase transitions. For P3 type layered $\text{K}_{2/3}\text{CoO}_2$ [7], multi-step phase transitions are also observed, although the delivered capacity ($\sim 60 \text{ mAh g}^{-1}$, 1.5–3.9 V) is somehow smaller than that of $\text{K}_{0.5}\text{MnO}_2$. Provided that $\text{K}_{0.5}\text{MnO}_2$ – $\text{K}_{0.5}\text{CoO}_2$ solid solution is formed, it is anticipated that those multiple phase transition can be mitigated so as to retain the resulting capacity for prolonged cycles. This tendency was first demonstrated by Ohzuku et al. [12] using LiCoO_2 – LiNiO_2 , namely, $\text{LiNi}_{0.5}\text{Co}_{0.5}\text{O}_2$ presenting a single-phase reaction during electrochemical reaction in Li cells. Employing the concept of one-to-one solid solution, we synthesize a $\text{K}_{0.54}[\text{Co}_{0.5}\text{Mn}_{0.5}]\text{O}_2$ compound of which the parent structure is a solid solution of $\text{K}_{0.5}\text{MnO}_2$ ($a = 2.875 \text{ \AA}$, $c = 19.085 \text{ \AA}$, $R3m$) and $\text{K}_{0.5}\text{CoO}_2$ ($a = 2.829 \text{ \AA}$, $c = 18.46 \text{ \AA}$, $R3m$) [7,8,13,14] that are stabilized in rhombohedral ($R3m$) structure. The incorporated Co^{3+} selectively replaces the Mn^{3+} in the $\text{K}_{0.54}[\text{Co}_{0.5}\text{Mn}_{0.5}]\text{O}_2$ ($a = 2.836 \text{ \AA}$, $c = 18.919 \text{ \AA}$, $R3m$) due to the same valence of Mn^{3+} and Co^{3+} rather than ionic size, which results in the decrease in the lattice parameters as a result of formation of solid solution. This $\text{K}_{0.54}[\text{Co}_{0.5}\text{Mn}_{0.5}]\text{O}_2$ balances the formation of Mn^{4+} in the $\text{K}_{0.54}[\text{Co}_{0.5}\text{Mn}_{0.5}]\text{O}_2$ compound. Based on the knowledge attained from LiCoO_2 , in addition, it is anticipated that the overlapping of the O2p orbital with the $\text{Co}^{3+/4+}$ redox enables facile electron transfer to lead cell operation at high rates. Less utilization of the $\text{Mn}^{4+/3+}$ redox pair and sharing of oxygen with CoO_6 octahedra like O–Mn–O–Co–O in the octahedral environment are predicted to minimize the JT distortion, while simultaneously improving the structural integrity upon cycling. Based on combined studies using *operando* X-ray diffraction and first-principles calculation, we confirmed that Co-substitution makes it possible to lower the structural deformation resulting from the JT distortion of Mn^{3+} in the oxide matrix and improve the structural stability, with a single-phase reaction during de/potassiation in the oxide lattice. As a result, the present P3- $\text{K}_{0.54}[\text{Co}_{0.5}\text{Mn}_{0.5}]\text{O}_2$ cathode exhibits a high reversible capacity, 120.4 mAh g^{-1} , with an average operating voltage of $\sim 2.85 \text{ V}$ (vs. K^+/K). Over 100 cycles at a 20 mA g^{-1} , up to 85% of its initial capacity is maintained. Even cycling test at 500 mA g^{-1} , the P3- $\text{K}_{0.54}[\text{Co}_{0.5}\text{Mn}_{0.5}]\text{O}_2$ displays an excellent power capability of 78 mAh g^{-1} , with a capacity retention of 62% for 500 cycles compared with the capacity measured at 20 mA g^{-1} . The first-principles calculations reveals that the low activation barrier energy of $\sim 260 \text{ meV}$ promotes the fast diffusion of K^+ ions in the P3- $\text{K}_x[\text{Co}_{0.5}\text{Mn}_{0.5}]\text{O}_2$ structure, which is

comparable to the activation barrier energy for Li^+ diffusion in conventional layered cathodes for LIBs. We, herein, report the excellent power capability of P3- $\text{K}_{0.54}[\text{Co}_{0.5}\text{Mn}_{0.5}]\text{O}_2$ as a promising cathode material for KIBs.

2. Experimental section

2.1. Material synthesis

The P3- $\text{K}_{0.54}[\text{Co}_{0.5}\text{Mn}_{0.5}]\text{O}_2$ powder was synthesized using a typical combustion method [15]. An aqueous solution was stoichiometrically prepared by dissolving KNO_3 , $\text{Co}(\text{NO}_3)_2 \cdot 6\text{H}_2\text{O}$, $\text{Mn}(\text{NO}_3)_2 \cdot 6\text{H}_2\text{O}$, and citric acid as a chelating agent in distilled water. The starting solution was evaporated overnight on a hot plate at $110 \text{ }^\circ\text{C}$ under constant stirring. Then, the dried powders were further heated to $200 \text{ }^\circ\text{C}$ for the auto-combustion of the citric acid. The as-received powders were calcined at $500 \text{ }^\circ\text{C}$ for 3 h to decompose the nitrates, and then re-calcined at $800 \text{ }^\circ\text{C}$ for 5 h under an air atmosphere at a heating rate of $2 \text{ }^\circ\text{C min}^{-1}$. This was followed by slow cooling at a cooling rate of $1 \text{ }^\circ\text{C min}^{-1}$. To prevent the formation of unwanted byproducts on the surface by moisture, the produced $\text{K}_{0.54}[\text{Co}_{0.5}\text{Mn}_{0.5}]\text{O}_2$ powders were promptly moved into an Ar-filled glove box [16].

2.2. Material characterization

To characterize the crystal structures of the synthesized powders, X-ray diffraction (XRD, Xpert, PANalytica) using Cu-K α radiation was performed. The XRD measurement was performed in the 2θ range of 10° – 80° with a step size of 0.03° . The FULLPROF Rietveld program was used to analyze the XRD patterns of the powders. The particle morphologies and sizes of the obtained precursors and powders were observed using scanning electron microscopy (SEM, JSM 6400, JEOL) and transmission electron microscopy (TEM, JEM2010, JEOL). To determine the stoichiometry of the $\text{K}_{0.54}[\text{Co}_{0.5}\text{Mn}_{0.5}]\text{O}_2$ compounds, energy-dispersive X-ray spectroscopy (EDX) mapping was used. To obtain the chemical composition to use Rietveld refinement, the as-synthesized powders were analyzed by ICP - AES (OPTIMA 8300, PerkinElmer). The powders samples were first dissolved in nitric and sulfuric acids (1:1 in volume), and of hydrofluoric acid (1/3 of the acid mixture in volume) was subsequently added. These solutions were continuously stirred at $80 \text{ }^\circ\text{C}$ for 5 h. The resulting solutions were transparent without any precipitates. The results of ICP-AES showed concentrations for K, Co, and Mn in average, as follow; $\text{K}_{0.537}[\text{Co}_{0.498}\text{Mn}_{0.502}]\text{O}_2$, which are close to the designated compositions of $\text{K}_{0.54}[\text{Co}_{0.5}\text{Mn}_{0.5}]\text{O}_2$. As shown Fig. S1, the $\text{K}_{0.54}[\text{Co}_{0.5}\text{Mn}_{0.5}]\text{O}_2$ is hygroscopic, so that hydrated phase appears after exposing in air one hour, seen in the XRD pattern measured exposing in air for 1 h. The direct volt-ampere method (CMT-SR1000, IT) was used to measure the DC electrical conductivity, in which a four-point probe was placed in contact with a disc sample. The K-storage mechanisms in the charge and discharge processes were examined by means of *ex-situ* XRD, *in operando* XRD, and *ex-situ* X-ray absorption spectroscopy (XAS). The *ex-situ* XAS measurements were carried out at the 6D beamline of the Pohang Accelerator Laboratory (PAL), Pohang, South Korea. The effects of the phase stability and redox behaviors during cycling are discussed based on these results.

2.3. Electrochemical tests

Electrodes were fabricated using a mixture of the active materials (80 wt%), conducting carbon (Super-P:KS-6 = 1:1, 10 wt%), and polyvinylidene fluoride (PVDF, 10 wt%) in *N*-methyl-2-pyrrolidone (NMP). The loaded slurry (approximately 3.0 – 4.0 mg cm^{-2}) was applied to Al foil and then dried overnight in an oven at $110 \text{ }^\circ\text{C}$ under vacuum before use. The electrochemical properties were determined using R2032 coin-type cells with potassium metal anodes separated by glass fiber (Advantec) in an Ar-filled glove box. The electrolyte solution

comprised a 0.5 M KPF₆ in ethylene carbonate (EC):diethyl carbonate (DEC) (1:1 by v/v). The assembled cells were charged/discharged between 1.5 V and 3.9 V at 25 °C. Galvanostatic intermittent titration technique (GITT) were performed by using R2032 coin-type cells with potassium metal anodes and the carbonated based electrolyte. After assembling cell, the GITT measurement of the electrode were conducted at a rate of 20 mA g⁻¹ with 30-min charge (depotassiation) or discharge (potassiation) step with 10-min rest and open-circuit periods of 1 h. Prior to fabricating hard carbon (Kureha) anode, pre-treatment of the hard carbon was done to eliminate adhered water at 1000 °C for 2 h in Ar atmosphere. After then, the hard carbon anode was fabricated by blending the active materials and PVDF (10 wt.%) with an appropriate amount of NMP solution. The obtained slurry was applied on copper foil and then dried at 80 °C in a vacuum oven. Discs were punched out of the dried electrodes (diameter: 16 φ, mass loading; ~1.8 mg cm⁻²) to assemble coin cells with the K metal anode for coin type half cells and with P3 type K_{0.54}[Co_{0.5}Mn_{0.5}]O₂ cathode for coin type full cells. The fabricated anodes were pre-sodiated through direct contact with potassium metal (Alfa Aesar) in 0.5 M KPF₆ in EC:DEC electrolyte for 1 h to minimize the irreversibility during sodiation process. The cathode and hard carbon anode (a capacity ratio of negative and positive electrodes to be ~1.2, namely, ~3 mg cm⁻² for the cathode and ~1.8 mg cm⁻² for the anode) were separated by a glass fiber separator in a R2032 coin cell. The used electrolyte in the coin full cell was approximately 150 μl.

2.4. Computational details

Density functional theory (DFT) calculations were performed using the Vienna ab initio simulation package (VASP) [17]. We used projector-augmented wave (PAW) pseudopotentials [18] with a plane-wave basis set. The Perdew–Burke–Ernzerhof (PBE) parametrization of the generalized gradient approximation (GGA) was used for the exchange-correlation function [19]. The GGA + U method [20] was adopted to address the localization of d-orbitals in Mn and Co ions, with U values of 3.9 and 3.4 eV, respectively, as determined in a previous report [21]. All of the calculations were performed with an energy cutoff of 500 eV until the residual forces in the system converged to less than 0.05 eV Å⁻¹ per unit cell. To obtain a convex hull plot for P3-K_x[Co_{0.5}Mn_{0.5}]O₂, the phase stability of the P3-K_x[Co_{0.5}Mn_{0.5}]O₂ compounds was investigated by generating all of the K configurations corresponding to specific K contents and calculating the formation energies. The cluster-assisted statistical mechanics (CASM) software [22] was used to generate all of the K/vacancy configurations for each composition, and 30 configurations with the lowest electrostatic energy for each composition were used for the DFT calculations. Nudged elastic band (NEB) calculations [23] were performed to determine the activation barrier for K⁺ diffusion in the P3-K_x[Co_{0.5}Mn_{0.5}]O₂ structure. We considered five intermediate states between the first and final images of a single K⁺ diffusion event. During the NEB calculations, all of the structures were allowed to relax with fixed lattice parameters.

3. Results and discussion

First, the chemical composition of the as-synthesized product was confirmed by inductively coupled plasma, K_{0.537}[Co_{0.498}Mn_{0.502}]O₂, which are close to the designated compositions of K_{0.54}[Co_{0.5}Mn_{0.5}]O₂. The structure of P3-K_{0.54}[Co_{0.5}Mn_{0.5}]O₂ was verified through Rietveld refinement of the X-ray diffraction (XRD). As shown in Fig. 1a, the crystal structure of K_{0.54}[Co_{0.5}Mn_{0.5}]O₂ is defined as a typical P3-type layered structure belonging to the R3m space group without impurity phases, which agrees with the simulated XRD pattern. The peaks between 17° and 30° are related to the Mylar film which used to seal the sample on the XRD holder. The calculated parameters are *a* = 2.836(3) Å and *c* = 18.919(5) Å. The other structural information on the present P3-K_{0.54}[Co_{0.5}Mn_{0.5}]O₂ is tabulated in Table S1 and visualized in

Fig. 1b. The calculated lattice parameters are slightly lower than those of K_{0.5}MnO₂ (*a* = 2.875 Å and *c* = 19.085 Å), but higher than those of K_{0.5}CoO₂ (*a* = 2.829 Å, *c* = 18.46 Å, R3m) [7,8,13]. In consideration of the above-mentioned results, K_{0.54}[Co_{0.5}Mn_{0.5}]O₂ is solid solution of the end members of K_{0.5}MnO₂ and K_{0.5}CoO₂. The electrical conductivity was 8.2 × 10⁻⁶ S cm⁻¹ as measured by a four-probe method. The X-ray absorption near-edge structure (XANES) spectra of the Mn and Co K-edges show that the average oxidation state of Mn is close to 4+ (Fig. 1c), while the substituted Co is stabilized at 3+ (Fig. 1d). In consideration of K_{0.5}MnO₂, which is composed of Mn³⁺ and Mn⁴⁺ with a ratio of 1 : 1, it was confirmed that the incorporated Co³⁺ preferentially replaces the Mn³⁺ because it has the same charge state rather than being the result of the ionic radii between Mn³⁺ (0.645 Å) and Co³⁺ (0.545 Å). Hence, it is reasonable that the replacement of Mn³⁺ by the smaller Co³⁺ results in a decrease in the lattice parameters for the K_{0.54}[Co_{0.5}Mn_{0.5}]O₂. The K atoms are accommodated at trigonal prismatic sites in the interslab space between MO₂ (M = Co, Mn) layers, and the O ions are stacked in the sequence order of ABBCA. The overall morphology of K_{0.54}[Co_{0.5}Mn_{0.5}]O₂ is shown in Fig. S3. Transmission electron microscopy (TEM) observations, along with the resulting energy dispersive X-ray spectroscopy (EDS) mappings, demonstrated that the P3-K_{0.54}[Co_{0.5}Mn_{0.5}]O₂ particles had the shape of hexagonal-platelets with an average diameter of 1.5–2 μm (Fig. 1e), and they consisted of the K, Co, and Mn elements (Fig. 1f). TEM image with EDS mapping data were rearranged to Fig. S4. The high resolution TEM (HR-TEM) image shows well-developed layers for the K_{0.54}[Co_{0.5}Mn_{0.5}]O₂, in which the interlayer distance agrees with the *d*-spacing of (003) plane (Fig. 1g). The selected-area electron diffraction (SAED) patterns along the [110] zone axis also confirms the symmetry stabilized in rhombohedral structure (inset of Fig. 1g).

Based on the structural data obtained from the Rietveld refinement of the XRD data and XANES, we performed a first-principles calculation to predict the theoretical properties of P3-K_x[Co_{0.5}Mn_{0.5}]O₂. Such K/vacancy configurations on P3-K_x[Co_{0.5}Mn_{0.5}]O₂ (0 ≤ *x* ≤ 1) were generated through the CASM software. Fig. 2a presents the convex-hull plot for the formation energies of P3-K_x[Co_{0.5}Mn_{0.5}]O₂ (0 ≤ *x* ≤ 1), and it was predicted that there were several stable intermittent phases between K₀[Co_{0.5}Mn_{0.5}]O₂ and K₁[Co_{0.5}Mn_{0.5}]O₂, which implies the single-phase reaction of P3-K_x[Co_{0.5}Mn_{0.5}]O₂ during de/potassiation processes. Furthermore, the first-principles calculation analyses indicated that, at a voltage range of 1.5–3.9 V (vs. K⁺/K), ~0.5 mol K⁺ ions can be reversibly de/intercalated from the P3-K_x[Co_{0.5}Mn_{0.5}]O₂ structure, which agrees with the experimental data observed in the result of galvanostatic intermittent titration technique (GITT) measurement (Fig. 2b). During the charging process, ~0.29 mol K⁺ ions are deintercalated from K_{0.54}[Co_{0.5}Mn_{0.5}]O₂ to form K_{0.25}[Co_{0.5}Mn_{0.5}]O₂. Then, ~0.5 mol K⁺ ions are intercalated to induce K_{0.75}[Co_{0.5}Mn_{0.5}]O₂ on discharge in the range of 3.9–1.5 V. Furthermore, it exhibits a smooth discharge curve, compared with K_xMnO₂ for KIBs [6,8]. It was reported that the JT distortion of Mn³⁺ deteriorating the structural stability in Na_xMnO₂ requires particular Na/vacancy configurations as a function of the Na content, which simultaneously causes the multiple voltage steps of Na_xMnO₂ during the charging/discharging process [24,25]. The smooth variation in the voltage profile is likely to mitigate not only the effect of K⁺/vacancy ordering but also the JT effect on Mn³⁺ at present, as a result of the replacement of Mn³⁺ by Co³⁺ in the crystal structure. It was reported that the JT distortion by Mn³⁺ results in difference of the partial Mn-O bond lengths compared with the other Mn-O bond lengths in MnO₆ octahedra, due to the certain electron configurations at the *d* orbital of Mn ion [26,27]. Thus, we supposed that verification of detailed information on the crystal structure should be required to verify suppression of the JT distortion by Mn³⁺ through Co-substitution. To obtain the thermodynamically stable structural information on the pristine P3-K_xMnO₂ and Co-substituted P3-K_x[Co_{0.5}Mn_{0.5}]O₂ (*x* = 0.75 and 0.25), we performed first-principles calculation with density functional theory (DFT), and then schematized

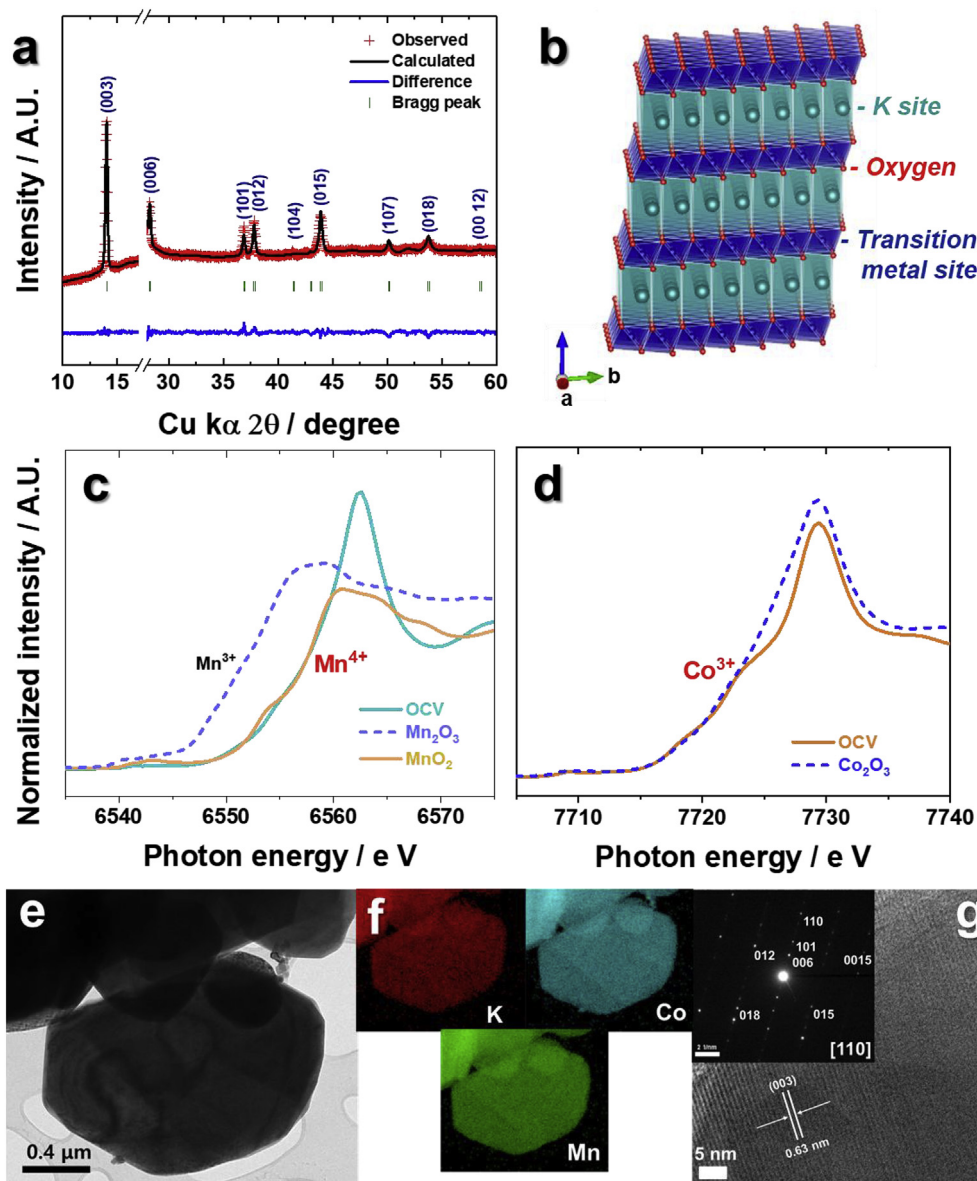


Fig. 1. (a) Rietveld refinement results for powder XRD patterns (Mylar film: $17^\circ \sim 30^\circ$), (b) illustration of $P3\text{-K}_{0.54}[\text{Co}_{0.5}\text{Mn}_{0.5}]\text{O}_2$ structure, (c) Mn K edge XANES spectra, (d) Co k edge XANES spectra with references (Mn_2O_3 , MnO_2 , and Co_2O_3), (e) TEM image, and (f) EDS mapping, and (g) HRTEM image of $\text{K}_{0.54}[\text{Co}_{0.5}\text{Mn}_{0.5}]\text{O}_2$ and the resulting SAED pattern observed along [110] zone axis.

the crystal structures of the $P3\text{-K}_x\text{MnO}_2$ and the $P3\text{-K}_x[\text{Co}_{0.5}\text{Mn}_{0.5}]\text{O}_2$ ($x = 0.75$ and 0.25) extracted from DFT calculation for comparison of the JT distortion by Mn^{3+} between $P3\text{-K}_x\text{MnO}_2$ and $P3\text{-K}_x[\text{Co}_{0.5}\text{Mn}_{0.5}]\text{O}_2$. Besides two types of Mn-O bonds exhibit longer distances than the others at MnO_6 octahedra in the pristine $P3\text{-K}_{0.75}\text{MnO}_2$ structure, all Mn-O bond lengths of MnO_6 octahedra in the Co-substituted $P3\text{-K}_{0.75}[\text{Co}_{0.5}\text{Mn}_{0.5}]\text{O}_2$ structure are similar to each other (Fig. 2c and d). However, unlike the $P3\text{-K}_{0.75}\text{MnO}_2$, the $P3\text{-K}_{0.25}\text{MnO}_2$ is composed of the MnO_6 octahedra in which all Mn-O bond lengths are similar, which indicates mitigation of the JT distortion by Mn^{3+} in $P3\text{-K}_x\text{MnO}_2$ structure (Fig. S5a). In case of $P3\text{-K}_x[\text{Co}_{0.5}\text{Mn}_{0.5}]\text{O}_2$, regardless of K contents in the structure, all Mn-O bond lengths in $P3\text{-K}_{0.75}[\text{Co}_{0.5}\text{Mn}_{0.5}]\text{O}_2$ and $P3\text{-K}_{0.25}[\text{Co}_{0.5}\text{Mn}_{0.5}]\text{O}_2$ are similar each other (Fig. S5b), which implies that Co-substitution is effective in mitigation of the JT distortion arising from Mn^{3+} in the structure. This difference may induce a smooth voltage profile for $P3\text{-K}_x[\text{Co}_{0.5}\text{Mn}_{0.5}]\text{O}_2$. To check the above explanation, electrochemical properties of $P3\text{-K}_{0.54}\text{MnO}_2$ and $P3\text{-K}_{0.54}[\text{Co}_{0.5}\text{Mn}_{0.5}]\text{O}_2$ were compared (Fig. S6). Several voltage plateaus were observed for the $P3\text{-K}_{0.54}\text{MnO}_2$ because of successive phase transition,

$P3 \rightarrow O3 \rightarrow X$ (O3-like phase) [8], while the $\text{K}_{0.54}[\text{Co}_{0.5}\text{Mn}_{0.5}]\text{O}_2$ showed the smooth voltage profiles that led to improvement in cycling performance.

The electrochemical activity for the $\text{K}_{0.54}[\text{Co}_{0.5}\text{Mn}_{0.5}]\text{O}_2$ was first investigated by cyclic voltammetry (CV) (Fig. 3a): i) between 1.5 and 4.3 V (red line) and 1.5 and 3.9 V (blue line) at a sweep rate of 0.5 mV s^{-1} . The anodic and cathodic reactions were highly reversible in the test range of 1.5 and 3.9 V, while irreversible anodic reaction was observed at higher potential over 4 V. Such irreversibility highlighted in inset is likely associated with oxidative decomposition of electrolyte; hence, we set the operation range from 1.5 to 3.9 V to minimize the effect of electrolyte during cycling test. Preliminary cell test done at those two ranges indicate better cycling stability for the latter case (Fig. 3b). Similar phenomena were also mentioned in earlier works [8,28,29]. From the above theoretical prediction and the resulting electrochemical charge-discharge curves, we confirm that the present $P3\text{-K}_{0.54}[\text{Co}_{0.5}\text{Mn}_{0.5}]\text{O}_2$ undergoes less structural transition during the electrochemical reaction, which may result in the improved rate capability and cycling stability. As shown in Fig. 3c and d, the P3-

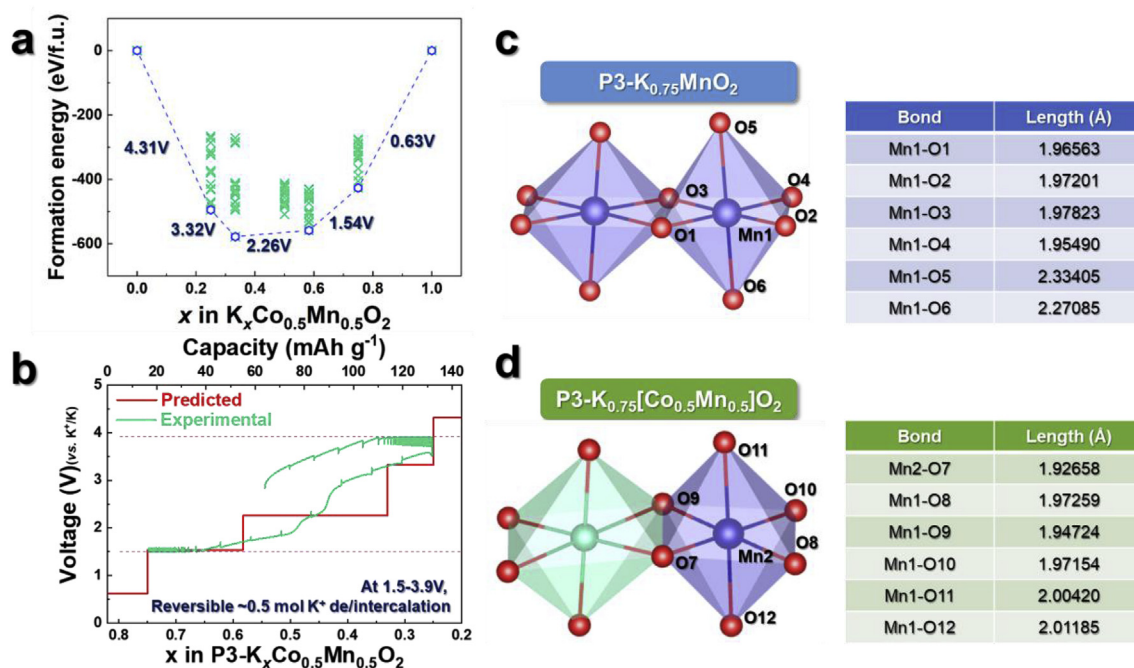


Fig. 2. (a) Formation energy of P3-K_x[Co_{0.5}Mn_{0.5}]O₂ (0 ≤ x ≤ 1), (b) comparison of experimentally measured GITT charge/discharge curve and predicted voltage profile, and comparison of Mn-O bonding distances between (c) P3-K_{0.75}MnO₂ and (d) P3-K_{0.75}[Co_{0.5}Mn_{0.5}]O₂.

K_{0.54}[Co_{0.5}Mn_{0.5}]O₂ electrode showed an acceptable power capability at rates to 500 mA g⁻¹. In particular, P3-K_{0.54}[Co_{0.5}Mn_{0.5}]O₂ delivered a discharge capacity of 78 mA h g⁻¹ at a rate of 500 mA g⁻¹ (full charge/discharge capacity in 20 min) and retained 65% of the capacity obtained at 20 mA g⁻¹ because of its high electronic conductivity (Table S1). Slight differences in the shape of the charge curves with increasing current may be related to the unoptimized electrolyte that results from side reaction between K metal and electrolytic solvent (Fig. 3c), as the similar phenomena were observed in literature [8,13,30–33]. In a cycling test, the P3-K_{0.54}[Co_{0.5}Mn_{0.5}]O₂ electrodes showed excellent capacity retention of 85% after 100 cycles at 20 mA g⁻¹ and 62% after 500 cycles at 500 mA g⁻¹ (Fig. 3e and Fig. S7). The deficiency of potassium in K_{0.54}[Co_{0.5}Mn_{0.5}]O₂ causes the lower charge capacity than discharge capacity, and it gives the first Coulombic efficiency approximately 180%. Except the first cycle, not only the present K_{0.54}[Co_{0.5}Mn_{0.5}]O₂ but almost of potassium cathode exhibit unstable Coulombic efficiency below 100% during cycling, indicating more capacity is delivered on charge than discharge [8–10,30]. According to recent work by Nazar et al. [34], there are the high reactivity such as unwanted side reaction between K metal and conventional carbonate solvent such as propylene carbonate (PC) or ethylene carbonate (EC)/diethyl carbonate (DEC). This causes formation of thick solid electrolytic interphase (SEI) layer, leading to increased charge transfer resistance with low coulombic efficiency. Electrochemical impedance spectra reflect the rise of charge transfer resistance during cycles, presumably ascribed to the side reaction of electrolyte (Fig. S8). The post-cycled electrode was mounted in an Ar-filled chamber for XRD measurement, so that there was no contact with air during sample handling and measurement (Fig. 4a). The obtained XRD pattern was refined by Rietveld method and compared with the as-synthesized P3-K_{0.54}[Co_{0.5}Mn_{0.5}]O₂ (Table S2). The results indicate that there is almost no change in the structure after the extensive cycles. The post-cycled K_{0.54}[Co_{0.5}Mn_{0.5}]O₂ still shows clear layer image in Fig. 4b, agreeing with the XRD pattern shown in Fig. 4a. The corresponding SAED patterns along the [110] zone axis is identical to the as-synthesized K_{0.54}[Co_{0.5}Mn_{0.5}]O₂ (Fig. 1g), indicating the excellent structural stability.

The good rate capability of P3-K_{0.54}[Co_{0.5}Mn_{0.5}]O₂ was confirmed

through the first-principles calculation using the nudged elastic band (NEB) method. Fig. 5a shows that, despite the large ionic size of K⁺, an activation barrier energy of ~260 meV was required for K⁺ diffusion in P3-K_{0.75}[Co_{0.5}Mn_{0.5}]O₂, which was comparable to those of the conventional cathode materials for LIBs. Moreover, by changing the combination of Mn and Co at transition metal sites in the structure, the partial K⁺ ions only required a very low activation barrier of ~170 meV for K⁺ diffusion. (Fig. 5b). Therefore, the high rate performance of the present K_{0.54}[Co_{0.5}Mn_{0.5}]O₂ is understood.

Based on the first-principles calculation data, the structural variation of P3-K_x[Co_{0.5}Mn_{0.5}]O₂ was predicted as a function of the K⁺ content in the structure. As seen in Fig. 6a, it is calculated that the c-lattice parameter of P3-K_x[Co_{0.5}Mn_{0.5}]O₂ increases from ~18.86 Å to ~19.63 Å as K⁺ ions are deintercalated from the crystal structure. This is due to a result of the oxygen-oxygen (O²⁻-O²⁻) repulsion arising from the formation of vacancies at the potassium sites, which implies the shift of the (003) peak toward a lower 2θ angle in the XRD pattern. This prediction of the structural change in P3-K_x[Co_{0.5}Mn_{0.5}]O₂ during K⁺ de/intercalation was clearly confirmed through the *operando* XRD analysis (Fig. 6b). All of the major diffraction peaks corresponding to the P3-type hexagonal structure with R3m symmetry were clearly observed. During charging, the (003) and (006) XRD peaks of P3-K_x[Co_{0.5}Mn_{0.5}]O₂ were monotonically shifted toward lower angles, and then these peaks moved back to their original positions at 2.5 V. This reversible behavior seemed to be due to the reversibility of the Co^{3+/4+} redox pair, because the average oxidation state of Mn is 4+, which means it is not able to further oxidize above 4+. Further lowering the discharge voltage to 1.5 V induced more peak shifts toward lower angles than the original peak positions of K_{0.54}[Co_{0.5}Mn_{0.5}]O₂. This is due to the occurrence of additional redox species as a result of the appearance of Mn^{4+/3+} reaction. The c-lattice parameter of P3-K_x[Co_{0.5}Mn_{0.5}]O₂ decreased monotonously from ~19.63 Å to ~18.86 Å during discharge (Fig. 6c), which agreed with the results of the first-principles calculation. In addition, it was verified that P3-K_x[Co_{0.5}Mn_{0.5}]O₂ experienced a reversible single-phase reaction with a continuous shift in the XRD peaks during the K⁺ de/intercalation process, confirming the phase stability of the K_x[Co_{0.5}Mn_{0.5}]O₂ (x = 0.25–0.75) as the P3 rhombohedral structure during

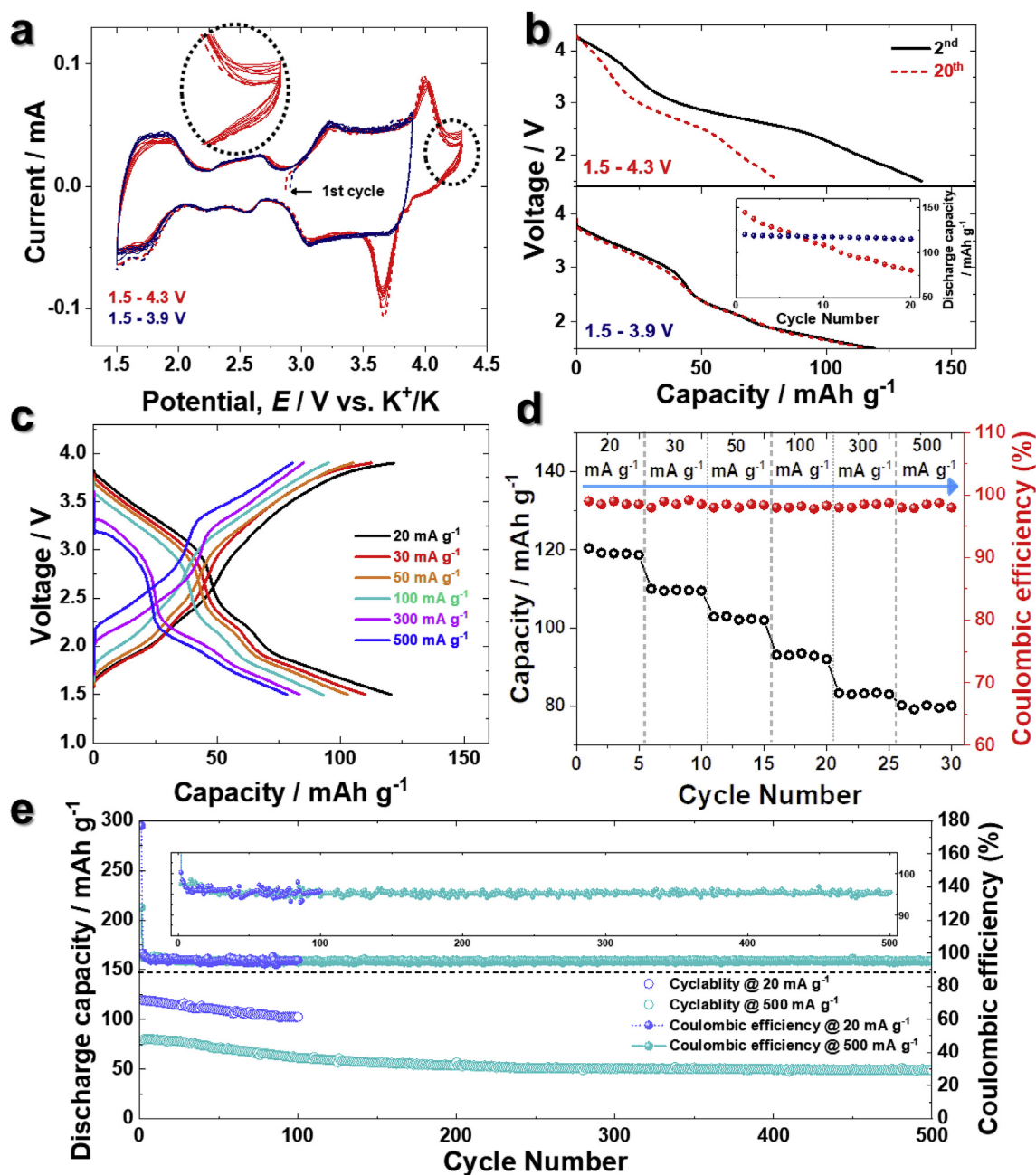


Fig. 3. (a) Cyclic voltammograms for $\text{K}_{0.54}[\text{Co}_{0.5}\text{Mn}_{0.5}]\text{O}_2$ tested in the range of 1.5–4.3 V and 1.5–3.9 V. (b) Comparison of upper cut-off voltage for 20 cycles: (top) 1.5–4.3 V and (bottom) 1.5–3.9 V (inset: cycling performance). (c) Capacity versus voltage curves measured at various currents (20 mA g^{-1} , 30 mA g^{-1} , 50 mA g^{-1} , 100 mA g^{-1} , 300 mA g^{-1} , 500 mA g^{-1}), (d) the resulting cyclability, (e) cycling performances at 20 mA g^{-1} for 100 cycles and 500 mA g^{-1} for 500 cycles.

electrochemical reaction. The phase stability was also confirmed in *ex-situ* XRD patterns for fully charged and discharged electrodes that the phases were identical to the fresh electrode, as shown in Fig. S9. This behavior is different from the previously reported P3-type K-based layered oxide cathodes that usually accompany the biphasic process [6–8,10]. It is thought that this simple structural variation is responsible for the improved electrochemical performances compared with those reported for layered cathode materials in Li systems such as $\text{Li}[\text{Ni}_{1/3}\text{Co}_{1/3}\text{Mn}_{1/3}]\text{O}_2$ [35,36] and $\text{Li}[\text{Ni}_{1/2}\text{Mn}_{1/2}]\text{O}_2$ [37,38]. More recently, Wang et al. [10] explained the importance of structural stability supported by a single-phase reaction of $\text{K}_{0.7}[\text{Fe}_{0.5}\text{Mn}_{0.5}]\text{O}_2$ for 1000 cycles in K cells.

The aforementioned K-storage process was explained with an *ex-situ* XANES analysis that demonstrated the chemical valence state and local

environment of the transition metals. To investigate the valence changes in the cobalt and manganese, the *ex-situ* XANES analysis was performed on various $\text{P3-K}_x[\text{Co}_{0.5}\text{Mn}_{0.5}]\text{O}_2$ samples ($x = 0.25, 0.54, 0.74$). The XANES spectra at the Mn and Co K-edges are shown in Fig. 7a and b, respectively. The Mn K-edge spectrum of the as-prepared $\text{P3-K}_{0.54}[\text{Co}_{0.5}\text{Mn}_{0.5}]\text{O}_2$ shows a profile similar to that of MnO_2 (Mn^{4+}). The oxidation state of the manganese in $\text{P3-K}_{0.54}[\text{Co}_{0.5}\text{Mn}_{0.5}]\text{O}_2$ is estimated to be the tetravalent state. A comparison of this spectrum with that of $\text{P3-K}_{0.25}[\text{Co}_{0.5}\text{Mn}_{0.5}]\text{O}_2$ shows that no significant changes are confirmed at the Mn K-edge. This suggests that the tetravalent manganese is not active under the charging process, as anticipated in Fig. 6b. Evident changes are seen for the Mn K-edge in the XANES spectra of the discharged $\text{P3-K}_{0.74}[\text{Co}_{0.5}\text{Mn}_{0.5}]\text{O}_2$. Specifically, the Mn K-edge absorption of $\text{P3-K}_{0.74}[\text{Co}_{0.5}\text{Mn}_{0.5}]\text{O}_2$ shifts to the lower energy

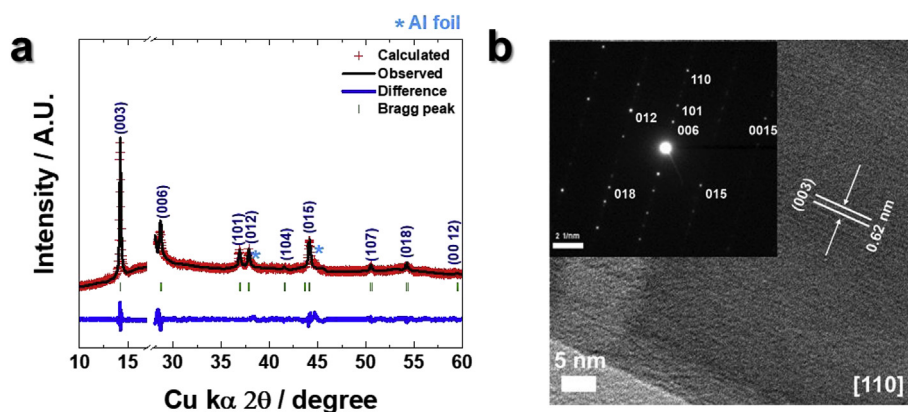


Fig. 4. (a) Rietveld refinement of XRD data for the post-cycled $K_{0.54}[Co_{0.5}Mn_{0.5}]O_2$ at 500 mA g^{-1} for 500 cycles, (Mylar film: $17^\circ \sim 30^\circ$), and (b) HRTEM image of the post-cycled $K_{0.54}[Co_{0.5}Mn_{0.5}]O_2$ and the resulting SAED pattern observed along $[110]$ zone axis.

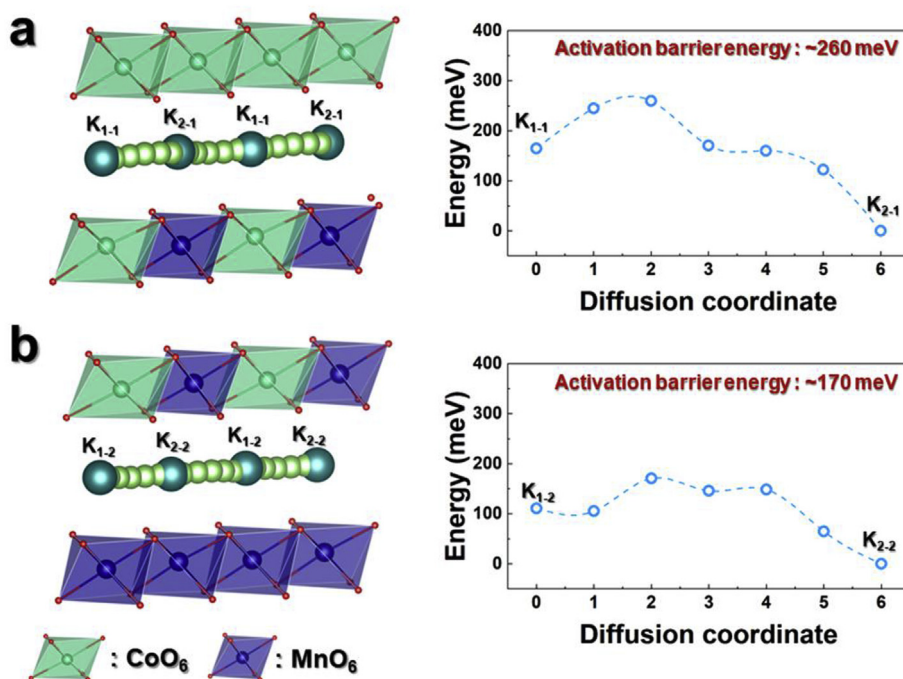


Fig. 5. (a) K_{1-1} - K_{2-1} and (b) K_{1-2} - K_{2-2} diffusion paths predicted with activation barrier energy on $P3-K_{0.75}[Co_{0.5}Mn_{0.5}]O_2$.

region compared to that of the as-synthesized $P3-K_{0.54}[Co_{0.5}Mn_{0.5}]O_2$, suggesting that the oxidation state of Mn moves to the trivalent state in $P3-K_{0.74}[Co_{0.5}Mn_{0.5}]O_2$ by an electrochemical reduction in the K cells. The Co K-edge spectra of $P3-K_{0.54}[Co_{0.5}Mn_{0.5}]O_2$ and Co_2O_3 (Co^{3+}) coincide with each other, suggesting that trivalent cobalt mainly exists in the octahedral environment in $P3-K_{0.54}[Co_{0.5}Mn_{0.5}]O_2$. The Co K-edge absorption of $P3-K_{0.25}[Co_{0.5}Mn_{0.5}]O_2$ clearly shifts to the higher-energy region compared to that of the as-synthesized $P3-K_{0.54}[Co_{0.5}Mn_{0.5}]O_2$. The spectrum is comparable in energy to that of CoO_2 (Co^{4+}) [39], indicating the oxidation of cobalt from the trivalent state in $P3-K_{0.54}[Co_{0.5}Mn_{0.5}]O_2$ to the tetravalent state in $P3-K_{0.25}[Co_{0.5}Mn_{0.5}]O_2$ by electrochemical oxidation in the K cells. A comparison of the spectra for the as-synthesized $P3-K_{0.54}[Co_{0.5}Mn_{0.5}]O_2$ and discharged $P3-K_{0.74}[Co_{0.5}Mn_{0.5}]O_2$ shows that no significant changes are observed at the Co K-edge, indicating that cobalt is in a reversibly reduced trivalent state on discharge. Local structural changes resulting from the $Mn^{3+/4+}$ and $Co^{3+/4+}$ redox reaction was verified by the *ex-situ* EXAFS results (Fig. S10). It is worth mentioning that the use of a high valence state for Mn above 3.5 + was necessary to minimize the effect of JT distortion in the MnO_6 octahedra. For this

purpose, we designed the chemical composition of the cathode material to be $K_{0.54}[Co_{0.5}Mn_{0.5}]O_2$, for which the oxidation state of Mn is $3.92+$. Because the Mn is close to $4+$, it does not participate in the electrochemical reaction during charging, whereas the reduction of Mn occurs in the range of 2.5–1.5 V on discharge, in which the reduction produces a Mn oxidation state of $3.52+$. Furthermore, although a half of the MnO_6 octahedra are composed of Mn^{3+} , they share oxygen with the CoO_6 octahedra so that the effect of JT distortion can be reduced compared with the discharged Mn-based electrode. This effect reflects the occurrence of the single-phase reaction during the K^+ extraction and insertion processes in the operation range of 1.5–3.9 V in the K cells. In addition, the incorporation of Co enables the minimization of the activation barrier as low as those of the conventional layered electrodes for LIBs.

$K_{0.54}[Co_{0.5}Mn_{0.5}]O_2$ active materials were observed before and after the extensive cycling test at 500 mA g^{-1} (Fig. 4 and S11). Compared with the fresh $K_{0.54}[Co_{0.5}Mn_{0.5}]O_2$ material, the cycled active materials were able to keep the original morphology, without deteriorious fracture or cracking of particles. It is likely that this morphological integrity is related to the smaller variation in the c-axis, approximately 4%,

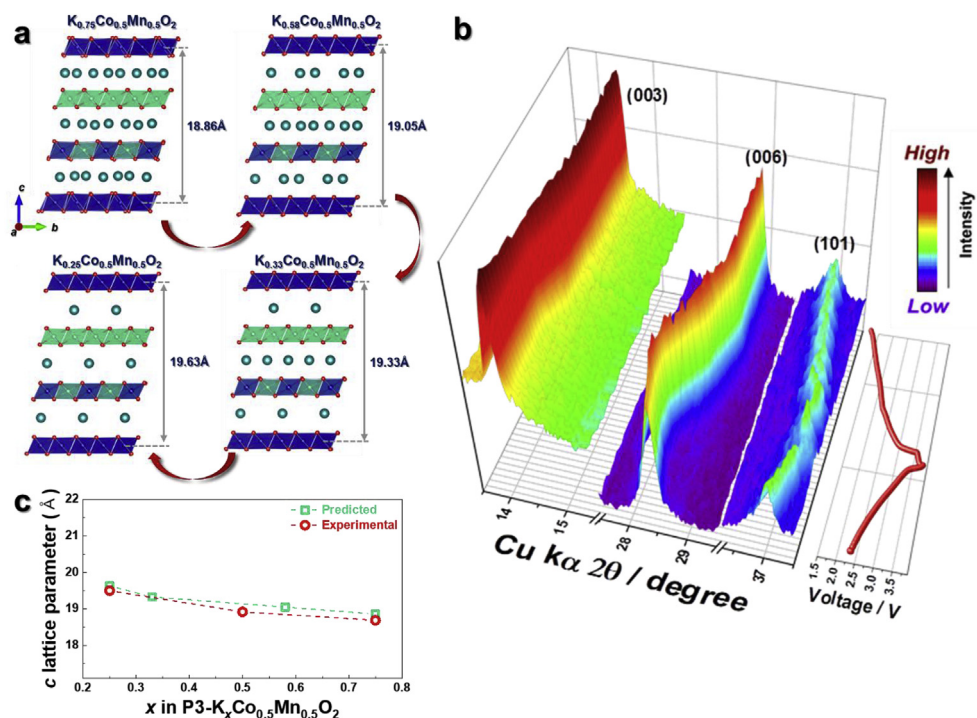


Fig. 6. (a) Predicted structural change in $\text{P3-K}_x[\text{Co}_{0.5}\text{Mn}_{0.5}]\text{O}_2$ ($0.25 \leq x \leq 0.75$), (b) *operando* XRD patterns of $\text{P3-K}_x[\text{Co}_{0.5}\text{Mn}_{0.5}]\text{O}_2$ with Kapton film: $17^\circ \sim 30^\circ$, and (c) comparison of c -lattice parameters of $\text{P3-K}_x[\text{Co}_{0.5}\text{Mn}_{0.5}]\text{O}_2$ obtained by first-principles calculations and *operando* XRD data.

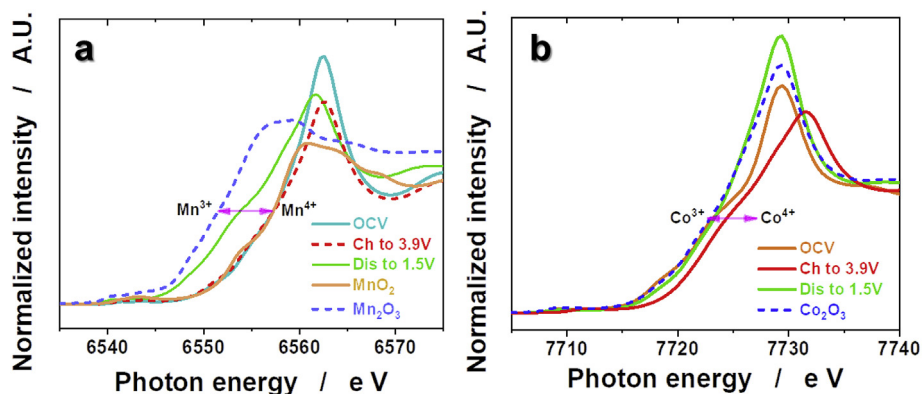


Fig. 7. XANES spectra of (a) Mn and (b) Co K-edge of $\text{P3-K}_x[\text{Co}_{0.5}\text{Mn}_{0.5}]\text{O}_2$ measured at the OCV with end of charge and discharge.

derived by the single-phase reaction during de/potassium shown in Fig. 6c and almost no change in the lattice parameters before and after 500 cycles at 500 mA g^{-1} (Table S2). Capacity fading is evident for long term cycling, and possible reasons are due to structural disintegration active materials and dissolution of active materials by HF. Since it is confirmed that the original phase P3 layered structure was maintained even after 500 cycles, ICP measurements were carried out for the post cycled electrode to check the dissolution of active materials in electrolyte for long cycles. The dissolved Mn and Co contents were 72 and 27 ppm, respectively. Such dissolution of active materials is likely responsible for the capacity decay for long term cycling. Similar results were observed in our previous work in Na system [40]. Also, instability between carbonate-based electrolyte and K metal may cause limit the capacity retention for long term [34], which should be resolved to improve the cell performances in K cells. The full cells configured between the $\text{K}_{0.54}[\text{Co}_{0.5}\text{Mn}_{0.5}]\text{O}_2$ and hard carbon were fabricated after an adjusting N/P capacity ratio of 1.2 to minimize the irreversibility and pre-cycled to formation of SEI layer on surface of hard carbon anode during few cycles for formation and grading processes (Fig. 8a) [25,41]. The full cell delivered a discharge capacity of approximately 96 mAh

(g-oxide) $^{-1}$, retaining $\sim 82\%$ of initial capacity for 100 cycles (Fig. 8b and c). This finding suggests great potential of $\text{K}_{0.54}[\text{Co}_{0.5}\text{Mn}_{0.5}]\text{O}_2$ cathode materials for application in KIBs.

In K system, layered structures are stable with K-deficient composition; namely K-deficient P2 and P3 structures. The present $\text{P3-K}_{0.54}[\text{Co}_{0.5}\text{Mn}_{0.5}]\text{O}_2$ shows that approximately a half of K site is vacant in the structure. Therefore, the extractable K^+ ion is limited during charge, while more amount of K^+ is inserted into the host structure during discharge. To balance this irreversible first capacity, more work should be done to explore other additives that provide additional amount of K^+ ions during the first charge. Our recent works have reported effective additives for Na-deficient compounds such as NaNO_2 for $\text{P2-Na}_{2/3}[\text{Co}_{0.05}\text{Mn}_{0.95}]\text{O}_2$ [41] and ethylenediaminetetraacetic acid (EDTA) tetra sodium salt for $\text{P2-Na}_{2/3}[\text{Al}_{0.05}\text{Mn}_{0.95}]\text{O}_2$ [42], of which both additives successfully compensated for the deficient Na^+ during the first charge that improve the first CE close to 100%. Further work will be carried out to find appropriate additives to compensate for the insufficient charge capacities for K-deficient P2 and P3 cathode materials.

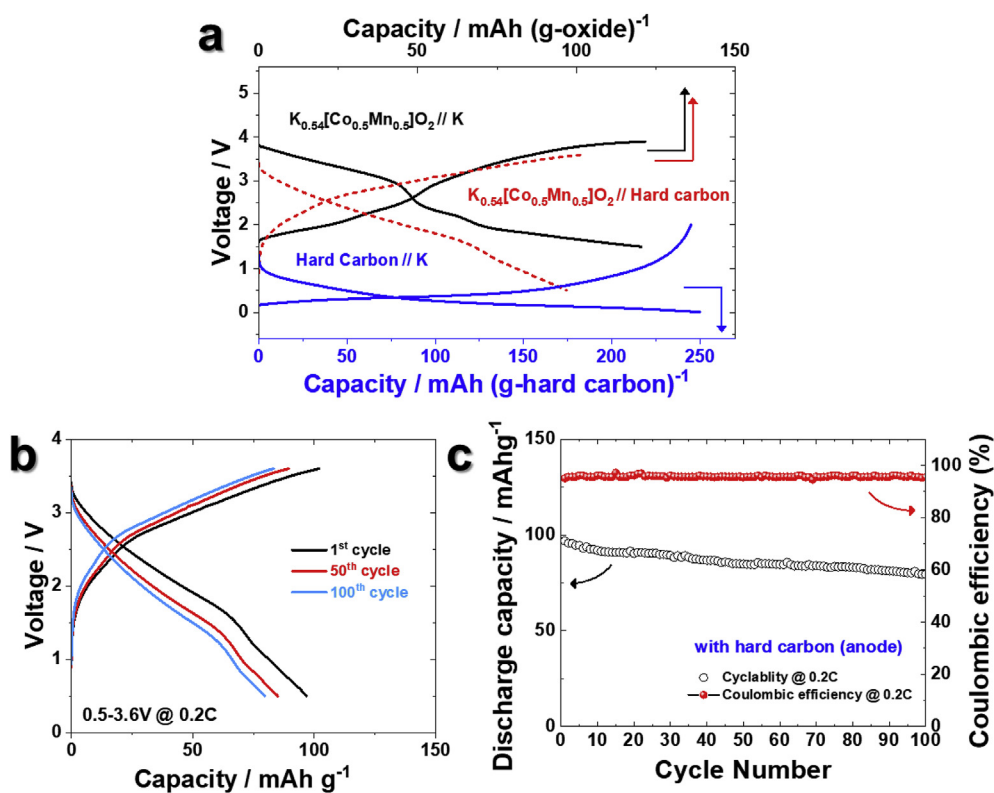


Fig. 8. (a) First charge and discharge curves of P3- $K_{0.54}[Co_{0.5}Mn_{0.5}]O_2//K$ metal half cell (black), P3- $K_{0.54}[Co_{0.5}Mn_{0.5}]O_2//$ hard carbon full cell (red), and hard carbon//K metal half cell (blue). Full cell performance of the P3- $K_{0.54}[Co_{0.5}Mn_{0.5}]O_2//$ hard carbon full cell; (b) charge-discharge curves (after formation and grading processes) and (c) cycling performance at 20 mA g^{-1} .

4. Conclusion

In summary, electrochemically reversible potassium extraction and insertion into/from P3-type $K_{0.54}[Co_{0.5}Mn_{0.5}]O_2$ is investigated for the first time. The overall potassium storage mechanism of P3- $K_{0.54}[Co_{0.5}Mn_{0.5}]O_2$ is investigated using a combination of electrochemical profiles, *operando* X-ray diffraction, *ex situ* XAS, and first-principles calculations. The P3- $K_{0.54}[Co_{0.5}Mn_{0.5}]O_2$ electrode delivers a high reversible capacity of 120.4 mAh g^{-1} in the voltage range of 1.5–3.9 V. On the basis of the *operando* X-ray diffraction, we confirm that P3- $K_{0.54}[Co_{0.5}Mn_{0.5}]O_2$ undergoes reversible structural changes with a single phase reaction upon the charge-discharge process in the voltage range of 1.5–3.9 V (vs. K^+/K). The co-existence of Co and Mn in the transition metal layer is highly effective at improving the structural stability by moderating the extent of the irreversible multiphase transformation, resulting in good stability for long term cycling and rate capability. Based on these results, we suggest that P3- $K_{0.54}[Co_{0.5}Mn_{0.5}]O_2$ has great potential as a promising candidate cathode material for advanced KIBs.

Acknowledgements

J.U.C. and J.K. and J.-Y.H. contributed equally to this work. This research was supported by the Basic Science Research Program through the National Research Foundation, funded by the Ministry of Science and ICT of Korea (NRF-2015M3D1A1069713), and supported by a National Research Foundation of Korea grant funded by the Korea government Ministry of Science and ICT of Korea (NRF-2017M2A2A6A01070834 and NRF-2017R1A2A2A05069634).

Appendix A. Supplementary data

Supplementary data to this article can be found online at <https://doi.org/10.1016/j.nanoen.2019.04.062>.

References

- [1] B. Dunn, H. Kamath, J.-M. Tarascon, Electrical energy storage for the grid: a battery of choices, *Science* 334 (2011) 928–935, <https://doi.org/10.1126/science.1212741>.
- [2] J.-Y. Hwang, S.-T. Myung, Y.-K. Sun, Sodium-ion batteries: present and future, *Chem. Soc. Rev.* 46 (2017) 3529–3614, <https://doi.org/10.1039/C6CS00776G>.
- [3] J.-Y. Hwang, J. Kim, T.-Y. Yu, S.-T. Myung, Y.-K. Sun, Development of P3- $K_{0.69}CrO_2$ as an ultra-high-performance cathode material for K-ion batteries, *Energy Environ. Sci.* 11 (2018) 2821–2827, <https://doi.org/10.1039/C8EE01365A>.
- [4] T. Deng, X. Fan, J. Chen, L. Chen, C. Luo, X. Zhou, J. Yang, S. Zheng, C. Wang, Layered P2-type $K_{0.65}Fe_{0.5}Mn_{0.5}O_2$ microspheres as superior cathode for high-energy potassium-ion batteries, *Adv. Funct. Mater.* 28 (2018) 1800219 <https://doi.org/10.1002/adfm.201800219>.
- [5] A. Eftekhari, Z. Jian, X. Ji, Potassium secondary batteries, *ACS Appl. Mater. Interfaces* 9 (2017) 4404–4419, <https://doi.org/10.1021/acsami.6b07989>.
- [6] C. Vaalma, G.A. Giffin, D. Buchholz, S. Passerini, Non-aqueous K-ion battery based on layered $K_{0.3}MnO_2$ and hard carbon/carbon black, *J. Electrochem. Soc.* 163 (2016) A1295–A1299, <https://doi.org/10.1149/2.0921607jes>.
- [7] Y. Hironaka, K. Kubota, S. Komaba, P2- and P3- K_2CoO_2 as an electrochemical potassium intercalation host, *Chem. Commun.* 53 (2017) 3693–3696, <https://doi.org/10.1039/C7CC00806F>.
- [8] H. Kim, D.-H. Seo, J.C. Kim, S.-H. Bo, L. Liu, T. Shi, G. Ceder, Investigation of potassium storage in layered P3-type $K_{0.5}MnO_2$ cathode, *Adv. Energy Mater.* 29 (2017) 1702480 <https://doi.org/10.1002/adma.201702480>.
- [9] C. Liu, S. Luo, H. Huang, Z. Wang, A. Hao, Y. Zhai, Z. Wang, $K_{0.67}Ni_{0.17}Co_{0.17}Mn_{0.66}O_2$: a cathode material for potassium-ion battery, *Electrochem. Commun.* 82 (2017) 150–154 <https://doi.org/10.1016/j.elecom.2017.08.008>.
- [10] X. Wang, X. Xu, C. Niu, J. Meng, M. Huang, X. Liu, Z. Liu, L. Mai, Earth abundant Fe/Mn-based layered oxide interconnected nanowires for advanced K-ion full batteries, *Nano Lett.* 17 (2017) 544–550, <https://doi.org/10.1021/acs.nanolett.6b04611>.
- [11] X. Wu, D.P. Leonard, X. Ji, Emerging non-aqueous potassium-ion batteries: challenges and opportunities, *Chem. Mater.* 29 (2017) 5031–5042, <https://doi.org/10.1021/acs.chemmater.7b01764>.
- [12] A. Ueda, T. Ohzuku, Solid-state redox reactions of $LiNi_{1/2}Co_{1/2}O_2$ ($R\bar{3}m$) for 4 volt secondary lithium cells, *J. Electrochem. Soc.* 141 (1994) 2010–2014, <https://doi.org/10.1149/1.2055051>.
- [13] H. Kim, J.C. Kim, M. Bianchini, D.-H. Seo, J. Rodriguez-Garcia, G. Ceder, Recent progress and perspective in electrode materials for K-ion batteries, *Adv. energy mater.* 8 (2017) 1702384 <https://doi.org/10.1002/aenm.201702384>.
- [14] C. Delmas, C. Fouassier, P. Hagenmuller, Les bronzes de cobalt K_xCoO_2 ($x < 1$). L'oxyde $KCoO_2$, *J. Solid State Chem.* 13 (1975) 165–171 [https://doi.org/10.1016/0022-4596\(75\)90114-0](https://doi.org/10.1016/0022-4596(75)90114-0).
- [15] J.U. Choi, Y.J. Park, J.H. Jo, L.-Y. Kuo, P. Kaghazchi, S.-T. Myung, Unraveling the

- role of earth-abundant Fe in the suppression of Jahn–Teller distortion of P2-Type $\text{Na}_{2/3}\text{MnO}_2$: experimental and theoretical studies, *ACS Appl. Mater. Interfaces* 10 (2018) 40978–40984, <https://doi.org/10.1021/acsmi.8b16522>.
- [16] C.-Y. Yu, J.-S. Park, H.-G. Jung, K.-Y. Chung, D. Aurbach, Y.-K. Sun, S.-T. Myung, NaCrO_2 cathode for high-rate sodium-ion batteries, *Energy Environ. Sci.* 8 (2015) 2019–2026, <https://doi.org/10.1039/C5EE00695C>.
- [17] G. Kresse, J. Furthmüller, Efficiency of ab-initio total energy calculations for metals and semiconductors using a plane-wave basis set, *Comput. Mater. Sci.* 6 (1996) 15–50 [https://doi.org/10.1016/0927-0256\(96\)00008-0](https://doi.org/10.1016/0927-0256(96)00008-0).
- [18] P.E. Blöchl, Projector augmented-wave method, *Phys. Rev. B* 50 (1994) 17953 <https://doi.org/10.1103/PhysRevB.50.17953>.
- [19] J.P. Perdew, K. Burke, M. Ernzerhof, Generalized gradient approximation made simple, *Phys. Rev. Lett.* 77 (1996) 3865 <https://doi.org/10.1103/PhysRevLett.77.3865>.
- [20] I.A. Vladimir, F. Aryasetiawan, A.I. Lichtenstein, First-principles calculations of the electronic structure and spectra of strongly correlated systems: the LDA + U method, *J. Phys. Condens. Matter* 9 (1997) 767–808, <https://doi.org/10.1088/0953-8984/9/4/002>.
- [21] A. Jain, G. Hautier, S.P. Ong, C.J. Moore, C.C. Fischer, K.A. Persson, G. Ceder, Formation enthalpies by mixing GGA and GGA + U calculations, *Phys. Rev. B* 84 (2011) 045115 <https://doi.org/10.1103/PhysRevB.84.045115>.
- [22] A. V. d. Ven, J.C. Thomas, Q. Xu, J. Bhattacharya, Linking the electronic structure of solids to their thermodynamic and kinetic properties, *J. Mat.* 80 (2010) 1393–1410 <https://doi.org/10.1016/j.matcom.2009.08.008>.
- [23] G. Henkelman, B.P. Uberuaga, H. Jónsson, A climbing image nudged elastic band method for finding saddle points and minimum energy paths, *J. Chem. Phys.* 113 (2000) 9901–9904 <https://doi.org/10.1063/1.1329672>.
- [24] S. Kumakura, Y. Tahara, K. Kubota, K. Chihara, S. Komaba, Sodium and manganese stoichiometry of P2-type $\text{Na}_{2/3}\text{MnO}_2$, *Angew. Chem. Int. Ed.* 55 (2016) 12760–12763, <https://doi.org/10.1002/anie.201606415>.
- [25] J.U. Choi, C.S. Yoon, Q. Zhang, P. Kaghazchi, Y.H. Jung, K.-S. Lee, D.-C. Ahn, Y.-K. Sun, S.-T. Myung, Understanding on the structural and electrochemical performance of orthorhombic sodium manganese oxides, *J. Mater. Chem. A* 7 (2019) 202–211, <https://doi.org/10.1039/C8TA08796B>.
- [26] H. Kim, G. Yoon, I. Park, K.-Y. Park, B. Lee, J. Kim, Y.-U. Park, S.-K. Jung, H.-D. Lim, D. Ahn, S. Lee, K. Kang, Anomalous Jahn–Teller behavior in a manganese-based mixed-phosphate cathode for sodium ion batteries, *Energy Environ. Sci.* 8 (2015) 3325–3335, <https://doi.org/10.1039/C5EE01876E>.
- [27] S. Wi, J. Park, S. Lee, J. Kang, T. Hwang, K.-S. Lee, H.-K. Lee, S. Nam, C. Kim, Y.-E. Sung, B. Park, Synchrotron-based x-ray absorption spectroscopy for the electronic structure of $\text{Li}_x\text{Mn}_{0.8}\text{Fe}_{0.2}\text{PO}_4$ mesocrystal in Li^+ batteries, *Nanomater. Energy* 31 (2017) 495–503 <https://doi.org/10.1016/j.nanoen.2016.11.044>.
- [28] B. Mortemard de Boisse, J.H. Cheng, D. Carlier, M. Guignard, C.J. Pan, S. Bordère, D. Filimonov, C. Drathen, E. Suard, B.J. Hwang, A. Wattiaux, C. Delmas, $\text{O}_3\text{-Na}_x\text{Mn}_{1/3}\text{Fe}_{2/3}\text{O}_2$ as a positive electrode material for Na-ion batteries: structural evolutions and redox mechanisms upon Na^+ (de), *J. Mater. Chem. A* 3 (2015) 10976–10989, <https://doi.org/10.1039/C4TA06688J>.
- [29] J. Yoshida, E. Guerin, M. Arnault, C. Constantin, B. Mortemard de Boisse, D. Carlier, M. Guignard, C. Delmas, New P2 - $\text{Na}_{0.70}\text{Mn}_{0.60}\text{Ni}_{0.30}\text{Co}_{0.10}\text{O}_2$ layered oxide as electrode material for Na-ion batteries, *J. Electrochem. Soc.* 161 (2014) A1987–A1991, <https://doi.org/10.1149/2.0121414jes>.
- [30] K. Sada, B. Senthilkumar, P. Barpanda, Electrochemical potassium-ion intercalation in Na_xCoO_2 : a novel cathode material for potassium-ion batteries, *ChemCommun* 53 (2017) 8588–8591, <https://doi.org/10.1039/C7CC02791E>.
- [31] R. Zhang, J. Bao, Y. Wang, C.-F. Sun, Concentrated electrolytes stabilize bismuth–potassium batteries, *Chem. Sci.* 9 (2018) 6193–6198, <https://doi.org/10.1039/C8SC01848K>.
- [32] K. Lei, F. Li, C. Mu, J. Wang, Q. Zhao, C. Chen, J. Chen, High K-storage performance based on the synergy of dipotassium terephthalate and ether-based electrolytes, *Energy Environ. Sci.* 10 (2017) 552–557, <https://doi.org/10.1039/C6EE03185D>.
- [33] X. Chen, X. Zhou, M. Hu, J. Liang, D. Wu, J. Wei, Z. Zhou, Stable layered P3/P2 $\text{Na}_{0.66}\text{Co}_{0.5}\text{Mn}_{0.5}\text{O}_2$ cathode materials for sodium-ion batteries, *J. Mater. Chem. A* 3 (2015) 20708–20714, <https://doi.org/10.1039/C5TA05205J>.
- [34] G. He, L.F. Nazar, Crystallite size control of prussian white analogues for nonaqueous potassium-ion batteries, *ACS Energy Lett* 2 (2017) 1122–1127, <https://doi.org/10.1021/acsenergylett.7b00179>.
- [35] M.H. Lee, Y.J. Kang, S.-T. Myung, Y.-K. Sun, Synthetic optimization of $\text{Li}[\text{Ni}_{1/3}\text{Co}_{1/3}\text{Mn}_{1/3}]\text{O}_2$ via co-precipitation, *Electrochim. Acta* 50 (2004) 939–948 <https://doi.org/10.1016/j.electacta.2004.07.038>.
- [36] K.M. Shaju, G.V. Subba Rao, B.V.R. Chowdari, Performance of layered $\text{Li}(\text{Ni}_{1/3}\text{Co}_{1/3}\text{Mn}_{1/3})\text{O}_2$ as cathode for Li-ion batteries, *Electrochim. Acta* 48 (2002) 145–151, [https://doi.org/10.1016/S0013-4686\(02\)00593-5](https://doi.org/10.1016/S0013-4686(02)00593-5).
- [37] M.V. Reddy, G.V. Subba Rao, B.V.R. Chowdari, Cathodic behaviour of NiO-coated $\text{Li}(\text{Ni}_{1/2}\text{Mn}_{1/2})\text{O}_2$, *Electrochim. Acta* 50 (2005) 3375–3382, <https://doi.org/10.1016/j.electacta.2004.12.011>.
- [38] S. Park, S.K. Kang, Y.C. Kang, Y.S. Lee, Y.-K. Sun, Preparation of layered $\text{Li}[\text{Ni}_{1/2}\text{Mn}_{1/2}]\text{O}_2$ by ultrasonic spray pyrolysis method, *Chem. Lett.* 32 (2003) 446–447 <https://doi.org/10.1246/cl.2003.446>.
- [39] Y. Koyama, H. Arai, Z. Ogumi, I. Tanaka, Y. Uchimoto, Co K-edge XANES of LiCoO_2 and CoO_2 with a variety of structures by supercell density functional calculations with a core hole, *Phys. Rev. B* 85 (2012) 075129 <https://doi.org/10.1103/PhysRevB.85.075129>.
- [40] A. Konarov, J.U. Choi, Z. Bakenov, S.-T. Myung, Revisit of layered sodium manganese oxides: achievement of high energy by Ni incorporation, *J. Mater. Chem. A* 6 (2018) 8558, <https://doi.org/10.1039/C8TA02067A>.
- [41] C.-H. Jo, J.U. Choi, H. Yashiro, S.-T. Myung, Controllable charge capacity using a

black additive for high-energy-density sodium-ion batteries, *J. Mater. Chem. A* 7 (2019) 3903–3909, <https://doi.org/10.1039/C8TA09833F>.

- [42] J.H. Jo, J.U. Choi, Y.J. Park, Z. Zhu, H. Yashiro, S.-T. Myung, New insight into ethylenediaminetetraacetic acid tetrasodium salt as a sacrificing sodium ion source for sodium-deficient cathode materials for full cells, *ACS Appl. Mater. Interfaces* 11 (2019) 5957–5965, <https://doi.org/10.1021/acsmi.8b18488>.



Ji Ung Choi is presently a Ph.D. candidate in the Department of NanoEngineering at Sejong University, South Korea, under the supervision of Professor Seung-Taek Myung. His research focuses on development of novel electrode materials in the fields of energy conversion and storage, such as cathode materials for Na, K-ion batteries.



Jongsoo Kim received Ph. D. (2014) at the Seoul National University (SNU) and is currently an assistant professor in the Department of Nanotechnology and Advanced Materials Engineering at Sejong University, South Korea. His research focuses on the development of new electrode materials for Li, Na, K-ion batteries using neutron/X-ray scattering with first-principle calculation.



Jang-Yeon Hwang received his Ph.D. degree (2018) on cathode materials for sodium ion batteries at Hanyang University. He is currently a postdoctoral fellow in the group of Prof. Yang-Kook Sun in the Department of Energy Engineering at Hanyang University, Korea. He has research interests in the development of next-generation energy-storage materials and systems. His research is focused on the development of novel electrode materials for high-energy Na, K-ion, and Li–sulfur batteries



Jae Hyeon Jo is presently a Ph.D. candidate in the Department of NanoEngineering at Sejong University, South Korea, under the supervision of Professor Seung-Taek Myung. His research focuses on materials development in the fields of energy conversion and storage, such as cathode and anode materials for Na, Zn, K-ion batteries.



Yang-Kook Sun received his M.S. degree and Ph.D. degree from the Seoul National University, South Korea. In 1996, he was a principal researcher at Samsung Advanced Institute of Technology and contributed to the commercialization of the lithium polymer battery. He has worked at the Hanyang University in Korea as a professor since 2000. His research covers development of new electrode materials for lithium ion batteries, sodium ion batteries, Li-S batteries, and Li-air batteries.



Seung-Taek Myung is a Professor of Department of Nanotechnology and Advanced Materials Engineering at Sejong University, South Korea. Before 2011, he affiliated at VK (principal engineer), 3 M (senior engineer), and Iwate University (assistant professor). He received his Ph.D. degree in Chemical Engineering from Iwate University, Japan, in 2003. His research interests include the development of electro-active materials and corrosion of current collectors of rechargeable lithium and sodium ion batteries.